Macromolecular Materials and Engineering
Open Access
www.mame-journal.de

Fabrication of Gentamicin Sulfate-Loaded 3D-Printed Polyvinyl Alcohol/Sodium Alginate/Gelatin-Methacryloyl Hybrid Scaffolds for Skin Tissue Replacement

*Muhammet Sefa Izgordu, Musa Ayran, Songul Ulag, Ridvan Yildirim, Berrak Bulut, Ali Sahin, Mehmet Mucahit Guncu, Burak Aksu, and Oguzhan Gunduz**

3D-printed scaffolds can better mimic the function of human skin, both biologically and mechanically. Within the scope of this study, the effect of the addition of different amounts (10, 15, 20 mg) of gentamicin sulfate (GS) to a 10 mL solution of natural and synthetic polymers is investigated. Sodium alginate (SA), gelatin-methacryloyl (GelMA), and polyvinyl alcohol (PVA) are chosen as bioactive materials. The surface morphology and pore structures are visualized by scanning electron microscopy (SEM). According to the results, it is observed that the pore sizes of all scaffolds are smaller than 270 µm, the lowest value (130 µm) is obtained in the scaffold loaded with 15 mg GS, and it also has the highest tensile strength value (12.5 ± 7.6 MPa). Similarly, it is observed that the tensile strength (9.7 ± 4.5 MPa) is high in scaffold loaded with 20 mg GS. The biocompatibility test is performed with fibroblast cells, and the results show that the scaffolds are biocompatible with cells. The antibacterial test is carried out against the *S.aureous* and *E. coli* and the results indicate that all GS-loaded scaffolds demonstrate antibacterial activity.

1. Introduction

The skin serves as the human body's first line of defense against physical, chemical, and biological threats. It has important vital functions, such as regulating body temperature and limiting water loss from the body.[1] Both mechanical flexibility and stability are required to execute these activities.[2] It is a complex structure consisting of three main layers, namely the epidermis, dermis, and hypodermis, which are composed of many sublayers, such as the superficial papillary dermis and the collagen-rich reticular dermis.[3,4] The dermis is mainly composed of collagen fibers and has a thickness ranging from 2 to 5 mm. The elastic fibers in the dermal layer provide elasticity and flexibility to the skin. The dermis also contains lymphatic and blood vessels, hair follicles, nerve endings, and sebaceous glands.[5] The main goal in burn management is increasing the survival of severely burned patients by rapid debridement and early closure of burn wounds, consequently reducing the infection risk. To achieve long-term recovery, certain properties of both dermal and epidermal layers of skin are important to incorporate. The clinical use of cultured skin substitutes for wound closure has reduced the amount of donor skin required by more than 10 times compared with conventional skin grafts. It has reduced the number of surgeries required to harvest donor skin while at the same time decreasing the time of recovery of severely burn-injured patients.[6] Tissue-engineered skin replacements have opened new horizons to deal with massive skin loss with cultured autologous keratinocyte grafts, cultured allogeneic keratinocyte grafts, autologous/allogeneic composites, acellular biological matrices, and cellular matrices, including such biological substances as fibrin sealant and various types of collagen,

M. S. Izgordu, M. Ayran, R. Yildirim, B. Bulut
Center for Nanotechnology & Biomaterials Application and Research (NBUAM)
Marmara University
Fahrettin Kerim Gokay, Istanbul 34722, Turkey

S. Ulag, O. Gunduz
Department of Metallurgical and Materials Engineering
Faculty of Technology
Marmara University
Fahrettin Kerim Gokay, Istanbul 34722, Turkey
E-mail: ucemogu@ucl.ac.uk

A. Sahin
Department of Biochemistry
School of Medicine/Genetic and Metabolic Diseases Research and Investigation Center
Marmara University
Maltepe Basıbuyuk, Istanbul 34854, Turkey

M. M. Guncu, B. Aksu
Department of Medical Microbiology
Faculty of Medicine
Marmara University
Maltepe Basıbuyuk, Istanbul 34854, Turkey

The ORCID identification number(s) for the author(s) of this article can be found under https://doi.org/10.1002/mame.202300151

DOI: 10.1002/mame.202300151

and hyaluronic acid.[5,6] Utilizing extrusion-based 3D printing technology which has many advantages, such as producing porous and complex structures that mimic natural architecture, providing vascularization, and it is unique to the person.[7,8] It is a fast and easy operation at low cost, ease of sterilization,[9] and precise printing of complex geometries with computer-aided design.[10] Polyvinyl alcohol (PVA) is generally used in biomedical applications due to its good biocompatibility, water-soluble, and nontoxicobility, and it can be crosslinked using X-ray irradiation.[11,12] Sodium alginate (SA) is a natural polymer that is biodegradable, biocompatible, inexpensive, and water-soluble. It is commonly used in tissue engineering studies to accelerate healing and increase tissue compatibility.[13] The physical and biological properties of gelatin-methacryloyl (GelMA), which is obtained by methacrylation of mainly primary amine groups of lysine amino acids, can be highly customized. Through cell-binding motifs such as arginylglycylaspartic acid (RGD) peptide in GelMA, it allows the proliferation of cells on its surface and spread within the scaffold. It also has low immunogenicity and excellent biocompatibility.[14] Antibiotics such as penicillin, vancomycin, and gentamicin are used to treat bacterial infections in tissue engineering.[15] Since GS has a broad spectrum of activity against both gram-positive and gram-negative bacteria and is frequently used to treat superficial skin infections.[16, 17]

In Kuo et al. study, they conjugated PVA, alginate (Alg), and gelatin (Gel) with methacrylic anhydride (MA) and were photo-crosslinked to fabricate PVAMA-AlgMA-GelMA hydrogel scaffolds utilizing a water-in-oil self-assembly technique. With different molar ratios of the polymer matrix, the swelling ratio, porosity, and cell entrapment in the hydrogel were examined in this study and results showed that the water content of the hydrogel was improved with the help from PVAMA, AlgMA, and GelMA, creating a hydrogel with high porosity that allowed induced pluripotent cells (iPSCs) to migrate more easily.[18] Therefore, this combination can be an ideal choice to bring enhanced properties to the structures.

In this study, our primary focus was on the development of GS-loaded 3D-printed scaffolds utilizing PVA, SA, and GelMA. Intriguingly, the combination of these components and their collective impact on a wide array of factors, including biological, morphological, chemical, rheological, and antibacterial aspects, has yet to be explored in the existing literature. We also delved into evaluating the optimal GS concentration within the scaffolds, which was comprehensively assessed by inspecting release profiles, antibacterial effectiveness, and fibroblast-based cell cultures. Additionally, we examined the crucial pre-printing consideration of hydrogel viscosity. Furthermore, we conducted a comprehensive examination of cell proliferation and attachment on the scaffolds, employing scanning electron microscope (SEM) imaging for elucidation.

2. Experimental Section

2.1. Materials

PVA (M_W = 89 000–98 000 Da, fully hydrolysed), SA (M_W = 21 600 Da), and GS were obtained from Sigma-Aldrich, and GelMA (M_W = 101 600 Da) was obtained from Collagen R&D company (Turkey). PVA was first dissolved in distilled water at a concentration of 13% w/v with 10 mL of solution at 90 °C on a magnetic stirrer at 500 rpm. After the PVA was completely dissolved and cooled to room temperature to prevent degradation of the natural polymers, 2% SA and 0.25% GelMA were added to the PVA solution. Lithium acyl phosphinate photoinitiator (LAP) was then added to the prepolymer solution, and a free radical reaction was then initiated by UV irradiation. LAP photoinitiator (0.025% w/v) was used for crosslinking GelMA under UV light (405 nm) to increase the mechanical properties and degradability of the PVA-SA-GelMA scaffolds. Finally, the GS was added to the PVA-SA-GelMA solution. Three different amounts of GS (10, 15, and 20 mg) were added to the solution. The composition percentages for each scaffold were presented in **Table 1**.

Table 1. The composition of the scaffolds

Name of the scaffolds	PVA [% w/v]	SA [% w/v]	GelMA [% w/v]	LAP [% w/v]	Amount of GS [mg]
PVA	13	—	—	—	—
PVA-SA	13	2	—	—	—
PVA-SA-GelMA	13	2	0.25	0.0025	—
PVA-SA-GelMA-10 GS	13	2	0.25	0.0025	10
PVA-SA-GelMA-15 GS	13	2	0.25	0.0025	15
PVA-SA-GelMA-20 GS	13	2	0.25	0.0025	20

2.2. Design and Production of the 3D-Printed Scaffolds

The scaffolds (20 × 20 × 1 mm^3) were designed in a 3D drawing program (Solidworks) and then converted to G-codes using Slic3r software. The scaffolds were produced using a piston-driven extrusion-based 3D printer (Hyrel 3D, SDS-5 Extruder, USA). The optimization studies were performed on parameters such as flow rate (1 mL h^{-1}) and infill density (96%) according to the viscosity of the solutions. All scaffolds were exposed to UV light for 10 s to crosslink after printing. Regarding the size of all scaffolds, the length was designed to be 20 mm, and after printing, their thicknesses were measured between 330 and 425 µm.

2.3. Characterization of the Scaffolds

The morphological characteristic was analyzed by SEM. Before SEM analysis, scaffolds were coated with gold for 90 s with a sputter coating machine (Quorum SC7620, ABD). The mean pore size was analyzed with the Olympus analysis software.

The chemical structure and functional groups of the scaffolds were determined using Fourier transform infrared spectroscopy (FTIR, JASCO-4000) equipped with an attenuated total reflection (ATR) unit. The spectrum was recorded in the transmittance mode at a wavelength between 4000 and 400 cm^{-1} with a resolution of 4 cm^{-1}.

A digital viscometer (CP 2000 Plus, Lamy Rheology, Champagne au Mont d'Or, France) was employed to assess the viscosity of the solutions across a range of shear rates from 0 to 1000 s^{-1} at room temperature before printing.

Thermal properties were analyzed by differential scanning calorimetry (DSC, Shimadzu). The scaffolds were placed in

closed aluminum pans, and the temperature was maintained from room temperature to 400 °C at a heating rate of 25 °C min^{-1}.

The tensile strength properties were investigated using a tensile test machine (Shimadzu, EZ-LX) to determine the mechanical properties of the 3D-printed scaffolds. The temperature, force, and speed parameters were set to 20 °C, 5 kN, and 5 mm min^{-1}, respectively. The scaffolds were directly put between the jaws of the device.

The swelling test was conducted on the 3D scaffolds. Equivalent portions of scaffold sections were standardized and subsequently inserted into tubes. To these tubes, phosphate buffer solution (PBS) with a pH of 7.4 was introduced. Over the course of the experiment, weight measurements were taken at 24 h intervals, while the PBS solution remained constant.

In vitro assessment was carried out to examine the release of GS from the scaffolds. The scaffolds loaded with 10, 15, and 20 mg of GS were individually weighed (5 mg each) and then transferred to separate tubes. These tubes were filled with 1 mL of PBS. The absorbance values were measured by a UV spectrometer (190–600 nm) by taking PBS from the samples kept in the thermal shaker at certain time intervals (15, 30, 60, 120, 180, 300 min, and 12, 24, 48, 72, and 96 h). Fresh PBS was used after each new measurement.

E. coli (ATCC 25 922) and *S. aureus* (ATCC 29 213) bacterial strains were cultured in columbia agar medium with 5% sheep blood. They were kept at 35–37 °C for 1 day for antimicrobial testing before preparing a cell suspension ($1–5 \times 10^8$ CFU mL^{-1}) in müller hinton Broth (MHB). The bacteria suspension was then spread on Müller Hinton agar 90 mm medium. After sterilization of the disc samples under UV, the samples and ampicillin control discs (2 and 10 µg) were transferred to the surface of the agar. After 24 h of incubation at 35 °C, the diameter of the growth inhibition zone around each disc was measured.

The scaffolds were cut using a mold that was designed to fit the dimensions of a 96-well plate. These cut scaffolds were then carefully placed into the wells of 96-well plates to test biocompatibility through in vitro cytotoxicity analysis. It was then sterilized overnight under UV irradiation. The experiment's duration, FBS, penicillin/streptomycin solution, and L-glutamine were added to Dulbecco's modified Eagle media (DMEM). Cytotoxicity was examined after culturing fibroblast cells (L929, 5×10^3 per well) onto scaffolds for predetermined intervals at 37 °C in a 5% CO_2 incubator. MTT (3-(4,5-dimethylthiazol-2-yl)−2,5-diphenyl tetrazolium bromide) test was applied to determine cell viability, and the measurements were repeated three times. The viability of fibroblast cells on the scaffolds was determined quantitatively by MTT analysis from the 1st day to the 3rd day. Following incubation, the scaffolds were washed three times with PBS solution, and all medium in the wells was removed. Afterward, the samples were washed, and 90 µL of fresh medium and 10 µL of MTT solution (5 mg mL^{-1} in PBS solution) were added and incubated for 3 h. After incubation, 100 µL of dimethyl sulfoxide (DMSO) was added to dissolve the formazan crystals, and the samples were again incubated for an additional hour. Then, the medium was removed from the wells, and absorbance values were measured at 540 nm.

Following the completion of cellular experiments, cell fixation was executed on the scaffolds. Subsequent to this, scaffolds underwent a 10 min incubation period at ambient temperature, while positioned on a shaker. Finally, the scaffolds were prepared for SEM imaging, which was conducted at 10 kV utilizing the EVO LS 10 SEM instrument by Zeiss. These images were used to examine the attachment and spreading of fibroblasts on the structures.

Statistical analyses were performed by Student's *t*-test with a 95% confidence interval. Measurements were performed three times and according to their mean values, the result was determined. The differences were considered significant at $p < 0.05$.

3. Results and Discussions

The fabricated scaffolds should have a 3D and interconnected porous structure for optimal cell adhesion, proliferation, nutrition, and gas transfer. In **Figure 1**, the graphical representation of 3D printed scaffolds is presented, including images of the scaffolds and corresponding optical microscopy images. The configuration of the surface and the structure of pores within the 3D-printed scaffolds hold significant importance in understanding their effects on wound healing within the field of tissue engineering.[19] According to Hutmacher et al., pore sizes smaller than 300 µm are suitable for permeability.[12] The pore structures of the scaffolds and the average pore size histograms are presented in **Figure 2**. The 3D scaffolds produced in this study were considered suitable for scaffold applications due to their average pore sizes of less than 300 µm. The average porous structure of PVA was found to be 136.99 µm (Figure 2a). A significant increase in pore size distribution was observed with the addition of the SA and GelMA (261.41 and 249.92 µm for PVA-SA and PVA-SA-GelMA, respectively) (Figure 2b,c). The smallest pore size (130.98 µm) among GS-added scaffolds was determined in PVA-SA-GelMA-15 GS scaffolds (Figure 2e). It was determined that the pore size of the PVA-SA-GelMA-15 GS scaffold was close to the pore size of the PVA scaffold.

The cohesiveness among the constituents of the scaffold plays a vital role in the 3D printing process, governing the creation of scaffolds and ensuring the stability of the resulting composite scaffolds. The molecular structure analyses of the scaffolds were performed with FTIR, and the results are shown in **Figure 3**. Within FTIR spectra of GS, distinct absorption bands manifest at characteristic wavenumbers, namely 1651, 1535, and 1120 cm^{-1}. These bands are attributed to specific functional groups present in the molecule: the absorption peak at 1651 cm^{-1} corresponds to the amide I band, indicative of the C═O stretching in the amide group; the absorption peak at 1535 cm^{-1} corresponds to the amide II band, signifying the N—H bending coupled with C—N stretching in the amide group, and the absorption peak at 1120 cm^{-1} corresponds to the HSO_4^- bond of the GS. The characteristic peak of GS also was observed at 635 cm^{-1} which is correlated to the SO_2 group.[20] In Figure 3b, three major absorption peaks were observed around 3260 cm^{-1} (O—H stretching), 2911 cm^{-1} (C—H stretching bond), and 1410 cm^{-1} (O—H bending) for PVA. A study revealed vibration peaks approximately at 1610 and 1350 cm^{-1}, aligning with the stretching vibration of carboxylate salt groups present in SA.[21] These findings closely parallel the results depicted in Figure 3c in this study. While analyzing the data, it becomes apparent that the characteristic peak of GS disappears upon its incorporation into the composite scaffolds at 635 cm^{-1} as depicted in Figure 3e,g. The disappearance of the SO_2

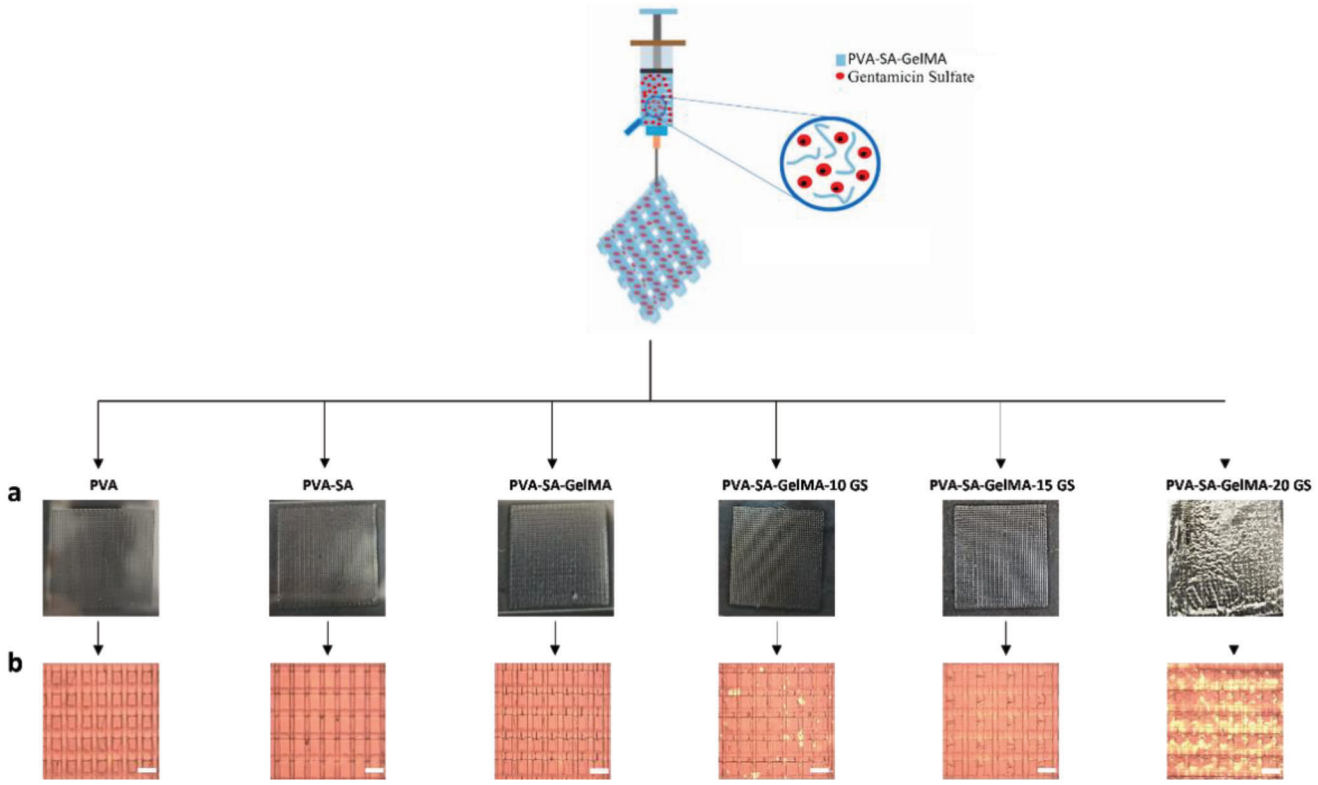

Figure 1. The visual depiction illustrates 3D printed scaffolds, with a) presenting scaffold images, and b) showcasing optical microscopy (bright field) images of the scaffolds.

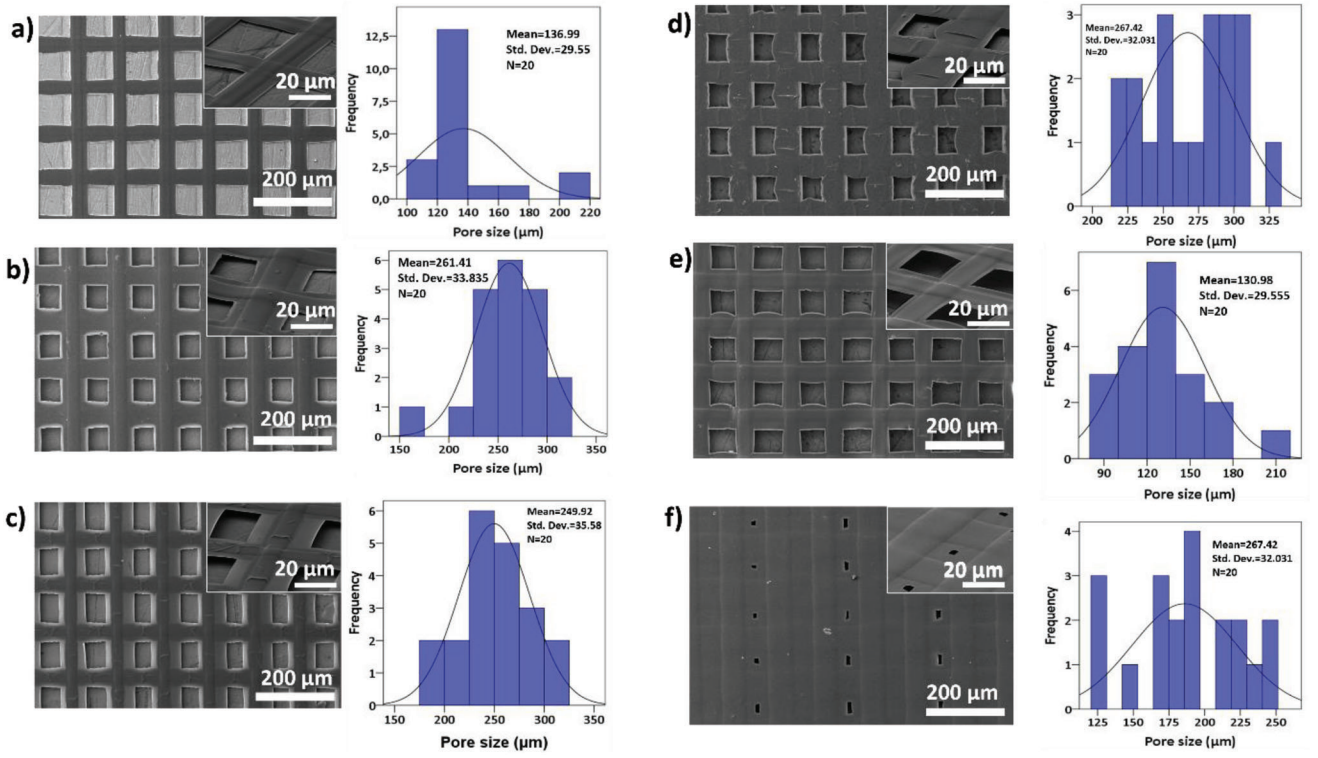

Figure 2. SEM images and pore size histogram of the scaffolds PVA a), PVA-SA b), PVA-SA-GelMA c), PVA-SA-GelMA-10 GS d), PVA-SA-GelMA-15 GS e), and PVA-SA-GelMA-20 GS f).

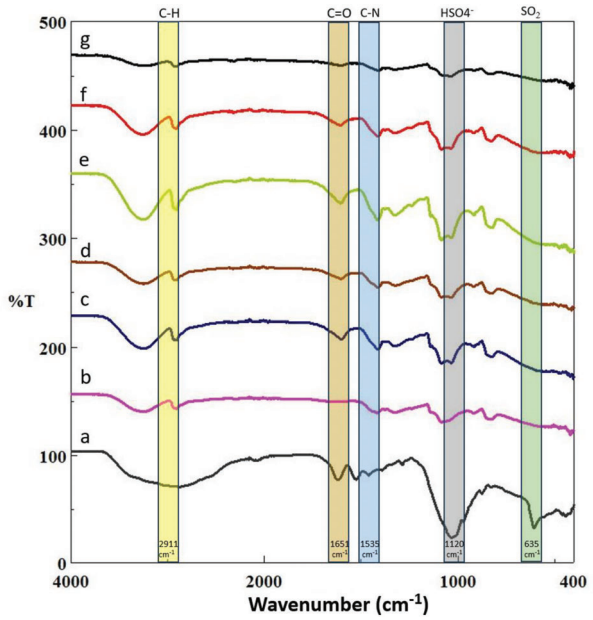

Figure 3. FTIR spectra of pure GS a) and all scaffolds: PVA b), PVA-SA c), PVA-SA-GelMA d), PVA-SA-GelMA-10 GS e), PVA-SA-GelMA-15 GS f), and PVA-SA-GelMA-20 GS g).

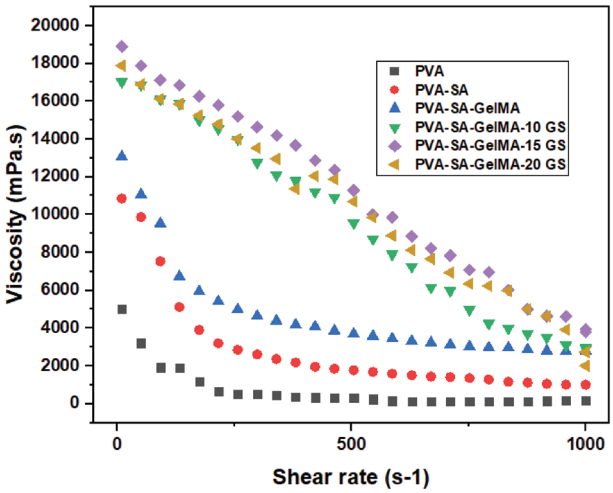

Figure 4. Exploring the rheological interplay of shear rate and viscosity in the hydrogel. This diagram elucidates the dynamic relationship between shear rate and viscosity within hydrogel structures.

peak might indicate modifications in the chemical environment of GS due to the incorporation of the other components, possibly affecting its molecular structure or local conformation. However, the relatively limited quantity of GS encapsulated within the PVA, SA, and GelMA might make it challenging to discern certain additional distinctive peaks associated with GS drug.

The primary physicochemical variables influencing the ability of hydrogels to be 3D printed include viscosity, shear force, shear rate, and so on. These variables are tied to the rheological characteristics of the hydrogels, which involve the study of material movement and deformation in response to external forces. The processes involved in extrusion-based bioprinting are closely intertwined with the rheological properties of the scaffolds.[16] There is an important approach that the viscosity of the substance utilized in 3D printing should be low enough to allow for efficient extrusion through the nozzle while still being strong enough for supporting the layer-by-layer structure.[22] The results were shown in **Figure 4**. Unfortunately, the viscosity values contain very high results. Although this is expected, it is due to the difficulty of initially rotating the hydrogel structure of the device in the center. As a result of its higher viscosity, PVA-SA-GelMA 20 GS was the solution that had the worst printing performance because of the fact that by making extrusion challenging high viscosity solutions impede printability.[22]

The results of the DSC analysis are presented in **Figure 5**. The DSC curves of the scaffolds were almost entirely similar. The peak in the 220 to 230 °C range is attributed to the melting point of the PVA,[23] and the peak at 300 °C is indicated the beginning of the decomposing of the PVA.[24] A slight increase in the melting point and decomposition temperature of PVA was seen with adding other polymers and drugs. T_g (glass transition temperature) and T_m (melting temperature) values of PVA are ≈81 and ≈220 °C, respectively.[12]

The mechanical properties of the scaffolds are given in **Table 2**. The mechanical properties of the PVA were decreased with the addition of the SA[25] and the addition of the GelMA to the binary structure at a very low percentage increased its tensile strength. When the effect of the drug on the mechanical properties of this structure was investigated, the highest mechanical properties of the scaffolds were determined at the PVA-SA-GelMA-15 GS scaffold. The PVA-SA-GelMA-20 GS is also one of the scaffolds with high tensile strength values. Since the elastic shear modulus of human skin varies between 2 and 8 kPa,[26] all scaffolds produced in this study are mechanically applicable. Typically, mechanical strength is known to have an inverse correlation with porosity.[27] In line with these findings of this, the investigation of the interaction between mechanical strength and porosity in GS-loaded scaffolds provided similar outcomes. The scaffold composed of PVA-SA-GelMA-15 GS exhibited the lowest pore dimensions as depicted in the SEM images, and the manifestation of such reduced pore dimensions significantly resulted in the attainment of the highest tensile strength across the diverse groups under investigation.

For tissue engineering, the water absorption property is an important parameter of the structures due to this circumstance, oxygen and nutrients can be transported.[22] **Figure 6** illustrates the water uptake ratios of structures at 37 °C. In this figure, both GS-containing and GS-free structures exhibit initial swelling up to the 3rd day, followed by the commencement of degradation by the conclusion of the 3rd day. It was revealed a consistent daily escalation in swelling rate across all drug-containing scaffolds, with each successive day experiencing a higher degree of swelling compared to the previous day, culminating in the establishment of equilibrium. Furthermore, the introduction of GelMA scaffolds was observed to amplify the swelling rate, consistent with findings from prior studies.[15] Also, although there was no significant difference between the drug-loaded scaffolds, PVA-SA-GelMA 20 GS had the highest swelling rate at the end of the 3rd day. The degradation of the structures after 3 days showed that the crosslinking agent ratio should be increased for further studies.

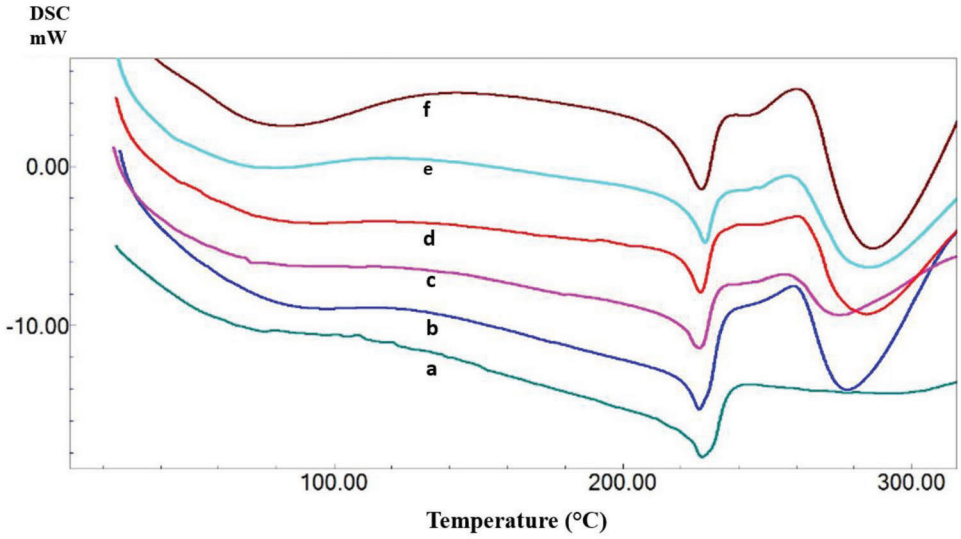

Figure 5. DSC thermograms for all scaffolds PVA a), PVA-SA b), PVA-SA-GelMA c), PVA-SA-GelMA-10 GS d), PVA-SA-GelMA-15 GS e), and PVA-SA-GelMA-20 GS f).

Table 2. Tensile test results of the scaffolds

Scaffolds	Tensile strength [MPa]	Strain at break [%]
PVA	7.4 ± 1.7	4.8 ± 1.6
PVA–SA	6.3 ± 2.5	3.8 ± 3.3
PVA-SA-GelMA	9.5 ± 7.4	2.5 ± 0.3
PVA-SA-GelMA-10 GS	5.3 ± 1.2	2.4 ± 0.1
PVA-SA-GelMA-15 GS	12.5 ± 7.6	5.3 ± 1.9
PVA-SA-GelMA-20 GS	9.7 ± 4.5	3.3 ± 0.9

The drug release study was performed at 37 °C in PBS (pH 7.4) to simulate the physiological conditions of the human body. In our preceding investigation, the calibration curve for GS was determined at a wavelength of 196 nm.[28] The cumulative release graph is given in **Figure 7**. Due to the water-soluble nature of PVA and SA polymers, the release of the drug took place rapidly, particularly within the initial 15 min interval. The application of antibiotics becomes crucial to halt the inflammatory phase at the injured site. Additionally, there arises a need for controlled antibiotic release, extending for a minimum of 7–8 h in the case of acute injuries, aiming to eliminate bacteria that might potentially infect the wound.[29] It is therefore important to observe that the release continues after 15 min of burst drug release. Although the drug release persisted throughout the entire examination period, it exhibited an accumulation of over 55% release in each scaffold within the initial 24 h. After 24 h, the PVA-SA-GelMA-10 GS scaffold released ≈58%, while the PVA-SA-GelMA-15 GS scaffold

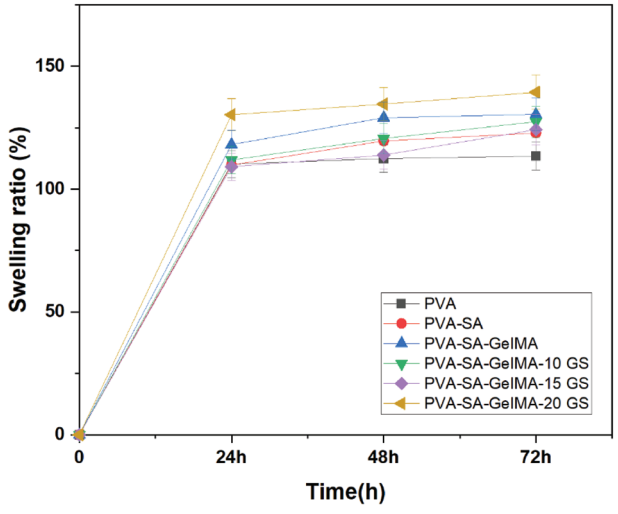

Figure 6. Swelling behaviors of all scaffolds.

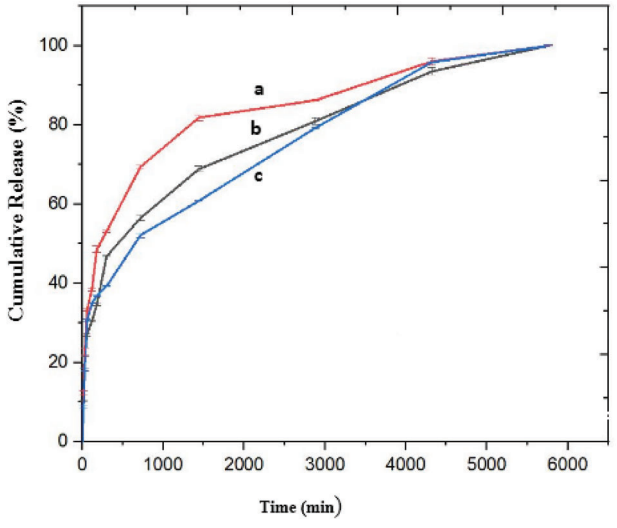

Figure 7. In vitro cumulative release profile of the GS from the scaffolds, PVA-SA-GelMA-10 GS a), PVA-SA-GelMA-15 GS b), and PVA-SA-GelMA-20 GS c).

Table 3. The zone diameter of the samples and ampicillin against *S. aureus* and *E. coli*

Scaffolds	*S.aureus* zone diameter [mm]	*E. coli* zone diameter [mm]
I-PVA	0	0
II-PVA-SA	0	0
III-PVA-SA-GelMA	0	0
IV-PVA-SA-GelMA-10 GS	5	7
V-PVA-SA-GelMA-15 GS	11	10
VI-PVA-SA-GelMA-20 GS	14	17
Amp-Ampicillin (2–10 µg)	15	17

released around 69%, and the PVA-SA-GelMA-20 GS scaffold released roughly 81%. The release of GS from all scaffolds occurred within 96 h. Likewise, Khodir et al.[30] investigated gentamicin-loaded nanofibers for controlled release in infection treatment, demonstrating 72 h efficacy, promising for infected wound therapy. As the concentration of GS increases, the graph indicates a reduction in the release rate. This can be attributed to the pores becoming more obstructed as the drug concentration rises. The increased drug ratio could lead to pore closure, potentially limiting diffusion. Consequently, the enlarged surface area might not facilitate diffusion as effectively, thus contributing to a diminished release rate.[31]

The antibacterial efficacy of the scaffolds was assessed through a disc diffusion technique, targeting *S. aureus* and *E. coli* bacteria. The antibacterial activity (zone diameter) of the scaffolds containing GS against *S aureus* and *E.coli* is shown in **Table 3** and **Figure 8**. The results unveiled the highest antibacterial efficacy of the scaffolds against *S. aureus* and *E. coli*, with 20 mg of GS-loaded scaffolds showing zone of inhibition diameters measuring 14 and 17 mm, respectively. Impressively, the antibacterial effect persisted even at the lowest GS usage level of 10 mg. The most optimal outcomes were observed within the scaffold infused with 20 mg of GS. This observation inherently demonstrated a proportional increase in the antibacterial efficacy of the scaffolds, corresponding with the escalating dosage of GS employed. Similarly, Gittard et al.[32] found that gentamicin-doped polyethylene glycol 600 diacrylate microneedles inhibited *S. aureus* growth, with a 26.8 mm inhibition zone confirming GS release. In another study, Sionkowska et al.[33] examined GS-loaded thin films, conducting microbiological tests to assess drug diffusion within the matrices, which revealed that the resultant films effectively restrained the growth of *E. coli* and *S. aureus* pathogens. The findings strongly support the potential utility of electrospun nanofibers as viable carriers for GS antibiotics in forthcoming tissue engineering applications. Considering that the release time of GS can extend up to 72 h in our study, prolonging the contact duration between the scaffolds and bacteria could further increase the antibacterial efficacy.[34] Moreover, the integration of GS into these structures can hold promise for burn cases, effectively inhibiting pathogenic activity and thereby serving as a preventive measure against infections at the site of injury.[35]

Cell viability assessments were conducted using the MTT test on days 1, 4, and 7 for all scaffolds, with the corresponding results presented in **Figure 9**. Particularly, no discernible toxic effects were observed across any of the scaffolds. Furthermore, the introduction of SA to the PVA matrix yielded distinct viability values on the 4 (92.4%) and 7 (76%) days, underscoring the influence of these polymers on longer-term cell behavior. Over the course of 7 days during the MTT test, the PVA-SA-GelMA scaffold treated with 20 mg of GS exhibited the highest cell viability (75.6%). In the case of the PVA-SA-GelMA-15 GS scaffold, it displayed the highest cell viability (76.8%) on the 1st day, maintained superior viability percentages over the initial 4 days (85%), but experienced a sharp decline in cell viability by the 7th day (62.1%) within the context of GS-loaded scaffolds. These findings underscore the dynamic interplay between drug dosage and cellular response, illuminating the intricate biological interactions at play. It was observed that there was no proportional correlation between

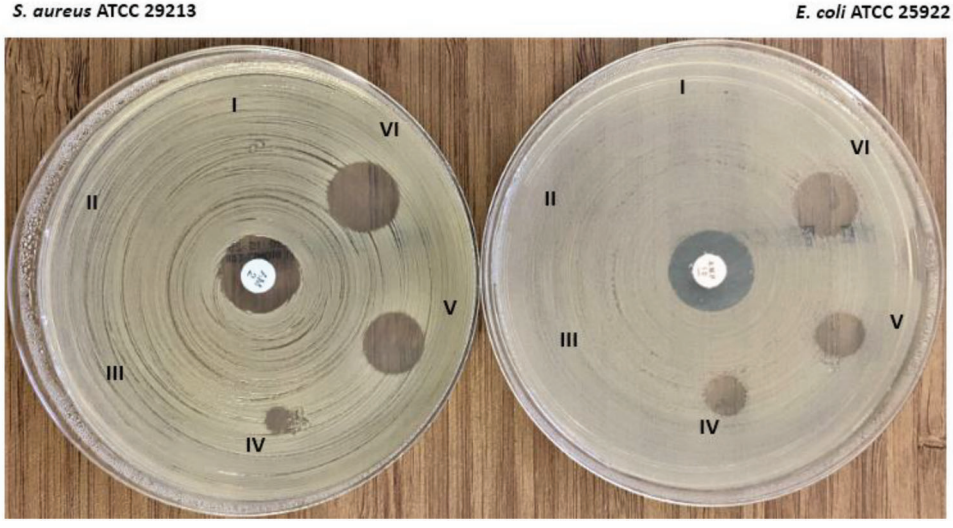

Figure 8. Inhibition zones of the scaffolds and ampicillin (2 and 10 µg) against *S. aureus* and *E. coli;* PVA (I), PVA -SA (II), PVA-SA-GelMA (III), PVA-SA-GelMA-10 GS (IV), PVA SA-GelMA-15 GS (V), and PVA -SA-GelMA-20 GS (VI).

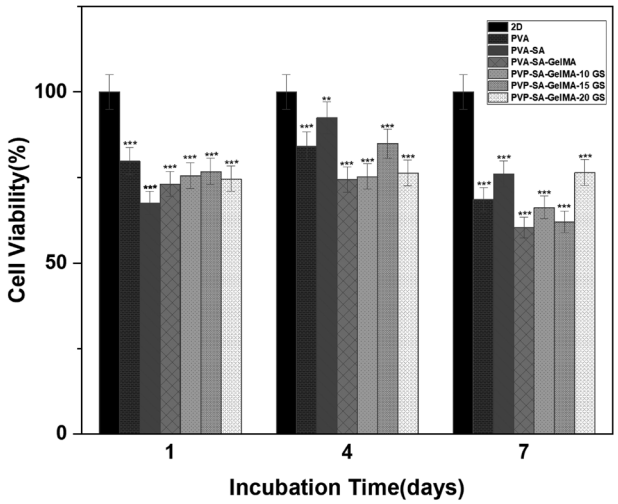

Figure 9. Cell viability of scaffolds compared to the control group (2D cells) after 1, 3, and 7 days of the culture period. One-way Analysis of Variance (ANOVA) Tukey–Kramer Multiple Comparisons Test, Comparison to 2D $^{**}p < 0.01$, $^{***}p < 0.001$.

the amount of GS and cell viability in the examined range. It was determined that the scaffolds did not make a statistically significant difference in cell viability. In Ulag et al.'s works, they fabricated gentamicin and fluconazole-added polymethylmethacrylate (PMMA) fibers for the treatment of corneal keratitis. According to the biocompatibility test performed with mesenchymal stem cells, they found that GS addition increased the viability of the cells.[28]

SEM analysis was performed to investigate the fibroblast cell attachment and morphology on scaffolds which is shown in **Figure 10**. According to the SEM images, it was possible to observe the cells attached and spread onto the surface of scaffolds. Cell-seeded scaffolds exhibited the presence of intricate cellular networks, a phenomenon evident across all scaffold samples, indicating that the biomaterial facilitated cell spreading and adhesion.

4. Conclusions

In this study, the scaffolds were produced effectively using the 3D printing technique. PVA, SA, and GelMA were chosen as based materials since they are biocompatible and water-soluble. GS, a broad-spectrum antibiotic, was added to 3D scaffolds in different amounts due to its ability to accelerate wound healing. Moreover, incorporating antibiotics like gentamicin into the scaffolds could prove advantageous for localized drug delivery, aiming to mitigate bacterial infections subsequent to surgery. The cytotoxicity tests revealed that scaffolds did not have any toxic effects on the fibroblast cells. The highest cell viability was determined at a scaffold loaded with 20 mg GS. This study provided evidence that 3D-printed GS-loaded PVA/SA/GelMA scaffolds can be a promising candidate for tissue engineering studies and burn treatments. Futhermore, GS-loaded scaffolds developed within this study offer promising potential in the field of tissue replacement, as they demonstrate the capacity to provide sustained antibiotic delivery, effectively eradicating and preemptively inhibiting bacterial infections caused by *E. coli* and *S. aureus* over an extended duration. This study provides the potential of 3D-printed GS-loaded PVA/SA/GelMA scaffolds as compelling properties for tissue engineering research, showcasing not only their antibacterial efficacy but also their favorable biological and morphological attributes.

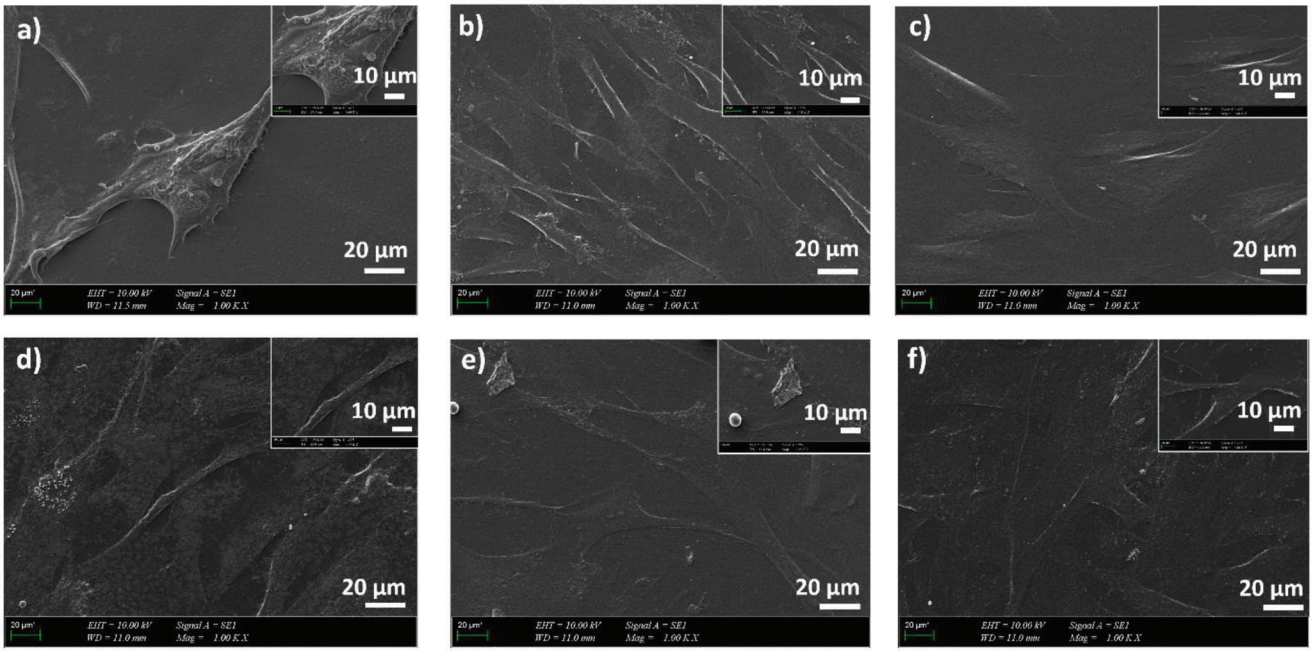

Figure 10. SEM images of scaffolds with fibroblast cells. PVA a), PVA-SA b), PVA-SA-GelMA c), PVA-SA-GelMA-10 GS d), PVA-SA-GelMA-15 GS e), and PVA-SA-GelMA-20 GS f).

Acknowledgements

This work was supported by the Research Fund of Marmara University as a 10376 Project Number.

Conflict of Interest

The authors declare no conflict of interest.

Author Contributions

Conceptualization (S.U., O.G.); Investigation (M.S.I., M.A.); Methodology (M.S.I., M.A., A.S., M.M.G., B.U.); Supervision (S.U., O.G.); Writing—original draft (M.S.I., S.U., M.A.); Writing—review & editing (O.G., S.U., M.A., B.B., R.Y.)

Data Availability Statement

The data that support the findings of this study are available from the corresponding author upon reasonable request.

Keywords

3D printing, alginate, gelatin, PVA, scaffold, skin tissue

Received: May 5, 2023
Revised: October 10, 2023
Published online:

[1] A. M. Croitoru, Y. Karacelebi, E. Saatcioglu, E. Altan, S. Ulag, H. K. Aydogan, A. Sahin, L. Motelica, O. Oprea, B. M. Tihauan, R. C. Popescu, D. Savu, R. Trusca, D. Ficai, O. Gunduz, A. Ficai, *Pharmaceutics* **2021**, *13*, 957.
[2] E. Altan, Y. Karacelebi, E. Saatcioglu, S. Ulag, A. Sahin, B. Aksu, A. M. Croitoru, C. I. Codrea, D. Ficai, O. Gunduz, A. Ficai, *Polymers* **2022**, *14*, 1971.
[3] F. M. Hendriks, D. Brokken, C. W. J. Oomens, D. L. Bader, F. P. T. Baaijens, *Med. Eng. Phys.* **2006**, *28*, 259.
[4] K. W. Ng, W. M. Lau, in *Percutaneous Penetration Enhancers Chemical Methods in Penetration Enhancement*, 1st ed. (Eds: N. Dragicevic, H. I. Maibach), Springer, Berlin **2015**, pp. 3–11.
[5] H. A. E. Benson, in *Topical and Transdermal Drug Delivery*, 1st ed. (Eds. H. A. E. Benson, A. C. Watkinson), John Wiley & Sons, Inc., Hoboken, NJ **2012**, pp. 1–22.
[6] T. Hakkarainen, R. Koivuniemi, M. Kosonen, C. Escobedo-Lucea, A. Sanz-Garcia, J. Vuola, J. Valtonen, P. Tammela, A. Mäkitie, K. Luukko, M. Yliperttula, H. Kavola, *J. Controlled Release* **2016**, *244*, 292.
[7] S. Ulag, S. Cesur, E. Dogan, M. Sengor, N. Ekren, C. B. Ustundag, O. Gunduz, *Gel-Inks for Tissue Engineering. Gels Horizons: From Science to Smart Materials* (Eds: A. Kumar, S. I. Voicu, V. K. Thakur), Springer, Singapore **2021**.
[8] S. Ulag, E. Uysal, T. Bedir, M. Sengor, N. Ekren, C. B. Ustundag, S. Midha, D. M. Kalaskar, O. Gunduz, *Polym. Adv. Technol.* **2021**, *32*, 3287.
[9] S. H. Kim, Y. K. Yeon, J. M. Lee, J. R. Chao, Y. J. Lee, Y. B. Seo, C. H. Park, *Nat. Commun.* **2018**, *9*, 1620.
[10] J. K. Placone, A. J. Engler, *Adv. Healthcare Mater.* **2018**, *7*, 1701161.
[11] Z. Zhang, W. Li, Y. Liu, Z. Yang, L. Ma, H. Zhuang, E. Wang, C. Wu, Z. Huan, F. Guo, J. Chang, *Bioact. Mater.* **2021**, *6*, 1910.
[12] D. W. Hutmacher, J. T. Schantz, C. X. F. Lam, K. C. Tan, T. C. Lim, *J. Tissue Eng. Regener. Med.* **2007**, *1*, 245.
[13] E. A. Kamoun, E.-R. S. Kenawy, X. Chen, *J. Adv. Res.* **2017**, *8*, 217.
[14] M. Kokabi, M. Sirousazar, Z. M. Hassan, *Eur. Polym. J.* **2006**, *43*, 773.
[15] L. Fan, H. Yang, J. Yang, M. Peng, J. Hu, *Carbohydr. Polym.* **2016**, *146*, 427.
[16] K. T. Shalumon, K. H. Anulekha, S. V. Nair, S. V. Nair, K. P. Chennazhi, R. Jayakumar, *Int. J. Biol. Macromol.* **2011**, *49*, 247.
[17] S. R. U. Rehman, R. Augustine, A. A. Zahid, R. Ahmed, M. Tariq, A. Hasan, *Int. J. Nanomed.* **2019**, *14*, 9603.
[18] Y.-C. Kuo, I.-H. Lee, R. Rajesh, *J. Taiwan Inst. Chem. Eng.* **2019**, *104*, 27.
[19] M. Ayran, A. Y. Dirican, E. Saatcioglu, S. Ulag, A. Sahin, B. Aksu, A. M. Croitoru, D. Ficai, O. Gunduz, A. Ficai, *Bioengineering* **2022**, *9*, 427.
[20] C. Dwivedi, H. Pandey, A. C. Pandey, P. W. Ramteke, *Curr. Nanosci.* **2015**, *11*, 222.
[21] Y. Jiang, Y. Hou, J. Fang, W. Liu, Y. Zhao, T. Huang, J. Cui, Y. Yang, Z. Zhou, *Int. J. Polym. Anal. Charact.* **2019**, *24*, 132.
[22] E. Ilhan, S. Cesur, E. Guler, F. Topal, D. Albayrak, M. M. Guncu, M. E. Cam, T. Taskin, H. T. Sasmazel, B. Aksu, F. N. Oktar, O. Gunduz, *Int. J. Biol. Macromol.* **2020**, *161*, 1040.
[23] R. K. Tubbs, *J. Polym. Sci. A* **1965**, *3*, 4181.
[24] A. K. Sonker, K. Rathore, R. K. Nagarale, V. Verma, *J. Polym. Environ.* **2018**, *26*, 1782.
[25] P. Kaur, V. S. Gondil, S. Chhibber, *Int. J. Pharm.* **2019**, *572*, 118779.
[26] S. Park, J. Tao, L. Sun, C.-M. Fan, Y. Chen, *Molecules* **2019**, *24*, 907.
[27] A. Tricoteaux, E. Rguiti, D. Chicot, L. Boilet, M. Descamps, A. Leriche, J. Lesage, *J. Eur. Ceram. Soc.* **2011**, *31*, 1361.
[28] O. Gunduz, S. Ulag, *Int. J. Polym. Mater. Polym. Biomater.* **2022**, *72*, 995.
[29] C. Kimna, S. Tamburaci, F. Tihminlioglu, *J. Biomed. Mater. Res. B: Appl. Biomater.* **2019**, *107*, 2057.
[30] W. Abdul Khodir, A. Abdul Razak, M. Ng, V. Guarino, D. Susanti, *J. Funct. Biomater.* **2018**, *9*, 36.
[31] Q. L. Loh, C. Choong, *Tissue Eng., Part B* **2013**, *19*, 485.
[32] S. D. Gittard, A. Ovsianikov, H. Akar, B. Chichkov, N. A. Monteiro-Riviere, S. Stafslien, B. Chisholm, C.-C. Shin, C.-M. Shih, S.-J. Lin, Y.-Y. Su, R. J. Narayan, *Adv. Eng. Mater.* **2010**, *12*, 77.
[33] M. Michalska-Sionkowska, B. Kaczmarek, M. Walczak, A. Sionkowska, *Mater. Sci. Eng. C* **2018**, *86*, 103.
[34] H. Abral, J. Ariksa, M. Mahardika, D. Handayani, I. Aminah, N. Sandrawati, S. M. Sapuan, R. A. Ilyas, *Polym. Test.* **2020**, *81*, 106186.
[35] S. Pisani, R. Dorati, E. Chiesa, I. Genta, T. Modena, G. Bruni, P. Grisoli, B. Conti, *Pharmaceutics* **2019**, *11*, 161.

